Realizing high-efficient oxygen reduction reaction in alkaline seawater by tailoring defect-rich hierarchical heterogeneous assemblies

Siqi Wu [a,b], Xiaobin Liu [a,b,*], Huimin Mao [a,b], Tong Cui [a,b], Bin Li [a], Guizhong Zhou [a,b], Lei Wang [a,b,c,*]

[a] Key Laboratory of Eco-chemical Engineering, International Science and Technology Cooperation Base of Eco-chemical Engineering and Green Manufacturing, Qingdao University of Science and Technology, Qingdao 266042, PR China
[b] College of Environment and Safety Engineering, Qingdao University of Science and Technology, Qingdao 266042, PR China
[c] College of Chemistry and Molecular Engineering, Qingdao University of Science and Technology, Qingdao 266042, PR China

ARTICLE INFO

ABSTRACT

The development of efficient and stable oxygen reduction reaction (ORR) electrocatalysts in seawater electrolyte is the key to realizing marine resource utilization and expanding metal-air battery applications. Herein, defect-rich Fe-doped Co nanoparticles encapsulated by N-doped hierarchical carbon (D-$_{Fe}$Co@NHC) are rationally designed and synthesized. It is worth mentioning that the Fe doping helps to promote the generation of metal defect and adjust the electronic structure of D-$_{Fe}$Co@NHC. Density functional theory (DFT) demonstrate that the metal defect and carbon defect jointly optimize the D-band center of D-$_{Fe}$Co@NHC. As a result, in alkaline seawater electrolyte, D-$_{Fe}$Co@NHC display a half-wave potential of 0.874 V, and the assembled liquid Zn-air battery exhibit a high peak power density (173 mW cm^{-2}) and ultra-long cycling stability (over 800 h). This work highlights the defect engineering in the construction of seawater-based oxygen reduction electrocatalysts, which provide a significant and promising approach for seawater-based metal-air cathode materials.

1. Introduction

As non-renewable energy sources become increasingly depleted, researchers are making many efforts to develop green energy storage and conversion technologies [1,2]. Zn-air batteries (ZABs) is considered as promising next-generation battery technologies for large-scale applications, owing to their high specific energy (1218 Wh kg^{-1}), high output voltage (1.66 V), and low expenses of Zn [3,4]. As is well-known, oxygen reduction reaction (ORR) is the core reaction of ZABs, and the Pt-based materials are the benchmark electrocatalyst for ORR [5,6]. Nevertheless, the scarcity of precious metals has severely limited the rapid development of ZABs [7–10]. Besides, almost all ZABs utilize the pure water as electrolyte, ignoring the abundant seawater resources. The application of seawater in the electrochemical energy conversion system is still in the early stage of exploration. The most important challenge is the competitive adsorption of chloride ions and oxygen containing substances on the active site, which will hinder the cathode activity of ORR [11–13]. In addition, corrosive chloride ions may lead to the corrosion of transition metal-based catalysts, which will adversely affect the stability of electrocatalytic materials, thus inhibiting the ORR process [14,15]. Therefore, seeking low-cost electrocatalyst with preeminent ORR performance in seawater electrolyte are crucial for the wide application of ZABs [16,17].

Defect engineering of electrocatalyst is an effective strategy to enhance ORR activity [18,19]. For instance, Kang and colleagues used a solid-state reaction strategy to prepare a metal-free carbon material (C-900) with defect sites [20]. The ORR catalytic performance of C-900 is better than that of commercial Pt/C in alkaline media. Besides, Zou and co-workers studied metal oxides and successfully introduced the metal vacancies of V_{Mn} and V_{Co} in situ into the bimetallic spinel MnxCo$_{3-x}$O$_4$ by thermal calcination [21]. The presence of metal defects (V_{Mn} and V_{Co}) enhances the ORR activity due to greatly enhanced electrical conductivity and O$_2$ adsorption capacity. To date, almost all studies are aiming at the single defect electrocatalyst, such as metal defect or carbon defect [22,23]. There is still a huge space for exploration and development of dual-defect-rich electrocatalyst with high-performance. Metal-organic frameworks (MOFs) is a class of inorganic-organic hybrid material [24–26], which can be in situ

---

* Corresponding authors at: Key Laboratory of Eco-chemical Engineering, International Science and Technology Cooperation Base of Eco-chemical Engineering and Green Manufacturing, Qingdao University of Science and Technology, Qingdao 266042, PR China.
E-mail addresses: liuxb@qust.edu.cn (X. Liu), inorchemwl@126.com (L. Wang).

transformed into functional metal species and porous carbon, giving a suitable platform to develop dual-defect-rich electrocatalyst [27,28].

Herein, we develop a facile strategy for constructing Fe-doped Co nanoparticles (FeCo) encapsulated by N-doped hierarchical carbon (NHC) with carbon and metal defect to boost ORR activity [29,30]. We demonstrate that Fe doping can not only tune the electronic structure of Co, but also induce more metal defect [31,32]. In alkaline seawater electrolyte, D-$_{Fe}$Co@NHC display an impressive half-wave potential ($E_{1/2}$) of 0.874 V, and the assembled liquid ZABs exhibit a high peak power density of 173 mW cm^{-2} and ultra-long cycling stability over 800 h. Density functional theory (DFT) demonstrate that the metal defect and carbon defect jointly optimize the electronic structure and D-band center of D-$_{Fe}$Co@NHC. What's more, the D-$_{Fe}$Co@NHC also exhibits great potential as an air cathode for seawater-based flexible quasi-solid-state ZABs, which can maintain a relatively stable charging and discharging platform under different bending angles.

2. Experimental section

2.1. Synthesis of CoFe-ZIF

First, 4 g 2-methylimidazole (2-MeIm) was dissolved in 60 mL deionized water to obtain a uniform aqueous solution (solution A). Meanwhile, 0.625 g Co(NO$_3$)$_2$·6 H$_2$O and 0.102 g FeCl$_2$·4 H$_2$O were dissolved in 20 mL deionized water (solution B). Then, the two solutions

were mixed together. After standing for 4 h, the mixed solution was centrifuged and dried overnight in an oven at 60 °C to obtain CoFe-ZIF.

2.2. Synthesis of $_{Fe}$Co@NHC

Dicyandiamide (C$_2$H$_4$N$_4$, 1.25 g) and CoFe-ZIF (0.5 g) were put in the upstream and downstream of tubular furnace, respectively. The precursor was heated to 350 °C at a ramp rate of 3 °C min^{-1}, held for 2 h in flowing Ar, and then the temperature was increased up to 800 °C for 2 h with a heating rate of 5 °C min^{-1}. After cooling to room temperature naturally, $_{Fe}$Co@NHC was obtained.

2.3. Synthesis of D-$_{Fe}$Co@NHC

$_{Fe}$Co@NHC (0.1 g) was dissolved in 4.0 M glacial acetic acid (15 mL) to obtain a mixed solution, which was heated in an oven at 70 °C for 6 h. The mixed solution was centrifuged and dried overnight in an oven at 60 °C to get D-$_{Fe}$Co@NHC. To explore the effect of acid concentration, D-$_{Fe}$Co@NHC-3 and D-$_{Fe}$Co@NHC-5 were prepared, with the acid concentrations of 3.0 M and 5.0 M, respectively.

Specific related experimental materials and test methods are provided in the Supporting Information.
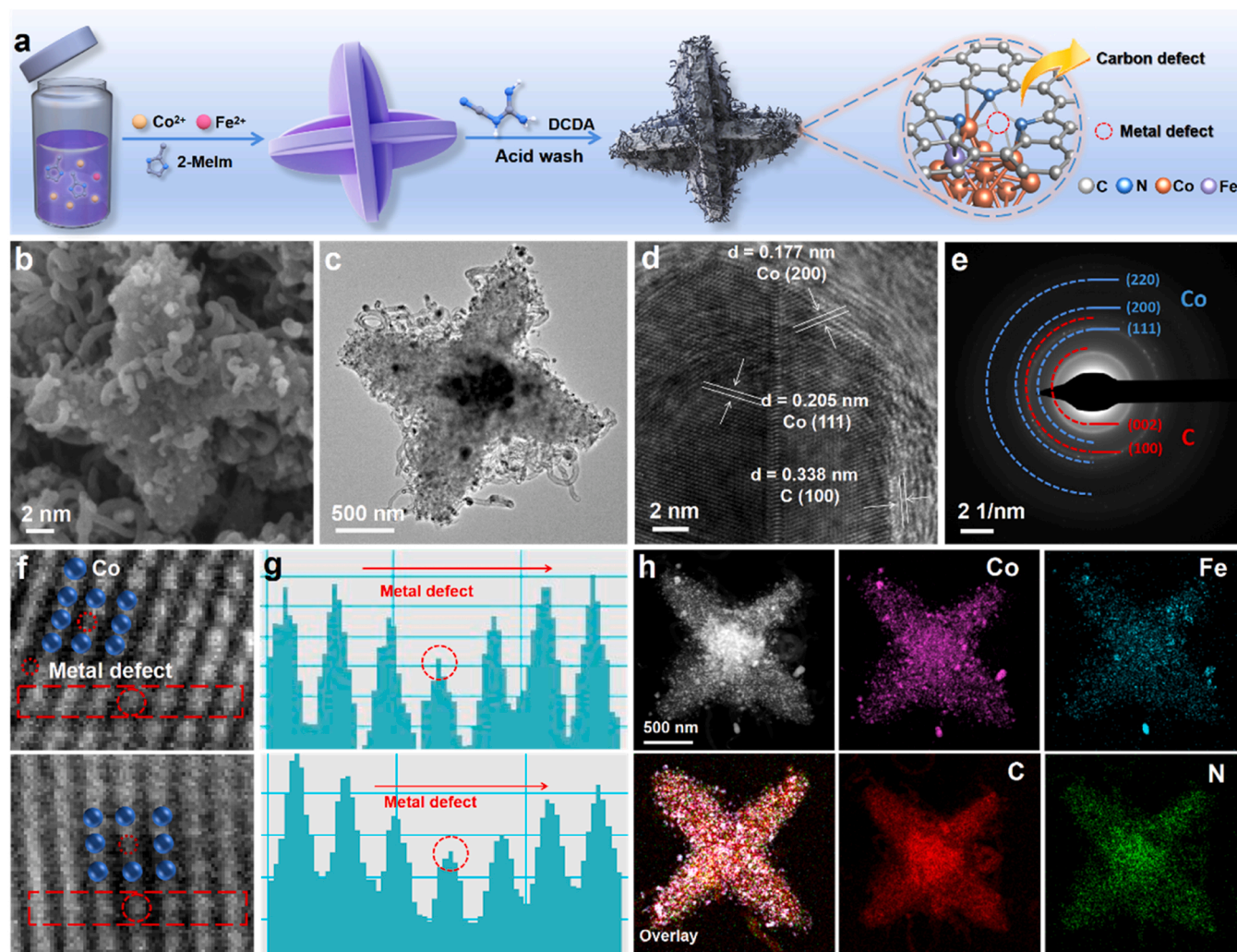
Fig. 1. a Schematic illustration of the synthesis route of D-$_{Fe}$Co@NHC. b SEM, c TEM, d HRTEM, e SAED pattern of D-$_{Fe}$Co@NHC. f HRTEM images and g corresponding intensity profile. h TEM mapping images of D-$_{Fe}$Co@NHC.

3. Results and discussion

3.1. Synthesis and characterization of D-*Fe*Co@NHC

The defect-rich Fe-doped Co nanoparticles encapsulated by N-doped hierarchical carbon are synthesized via a three-step process, as indicated in Fig. 1a. Scanning electron microscopy (SEM) (Fig. S1) shows that CoFe-ZIF presents a standard cruciform polyhedron morphology. After the carbonization process at high-temperature, abundant carbon nanotubes (CNTs) are in-situ grown on the surface of cruciform polyhedron with the assistance of dicyandiamide, noted as *Fe*Co@NHC (Fig. S2). Finally, the D-*Fe*Co@NHC is obtained after acid soaking of 4 M glacial acetic acid. It should be noted that the D-*Fe*Co@NHC still keep the stable hierarchical structure with CNTs embedded in the cruciform polyhedron (Fig. 1b), which is further proved by the transmission electron microscopy (TEM) images shown in Fig. 1c. Additionally, D-*Fe*Co@NHC-3 and D-*Fe*Co@NHC-5 also maintain their cruciform polyhedron after impregnated in 3 M and 5 M glacial acetic acid, respectively (Figs. S3–4). As is well-known, the construction of 1D/3D hierarchical structure can effectively accelerate the electron transfer, and ensure the sufficient contact between electrolyte and catalyst during the electrocatalysis process [33]. High-resolution TEM (HRTEM) image reveals that D-*Fe*Co@NHC possesses a typical core-shell structure with metal nanoparticles embedded in carbon matrix, which is beneficial to improve the electrical conductivity and corrosion resistance of catalyst (Fig. 1d and Fig. S5). The lattice fringes of 0.205 and 0.177 nm are ascribed to the (111) and (200) planes of metallic Co, and the lattice fringe of 0.337 nm corresponds to the (002) facet of graphite carbon layers. Selected area electron diffraction (SAED) (Fig. 1e) further proves the coexistence of Co and carbon phase, which is the same as the HRTEM result. To verify the existence of metal defect, the Fourier transform and inverse Fourier transform was carried out based on the HRTEM image (Fig. 1f). The metal defect is clearly observed by extracting the related line profiles in Fig. 1g. Meanwhile, the Co and Fe content of D-*Fe*Co@NHC was tested by inductively coupled plasma atomic emission spectroscopy (ICP-AES), in which Co:Fe = 15:1 (Table S1), the elemental mapping analysis in Fig. 1h discloses the homogeneous distribution of Co, Fe, C, and N elements throughout the whole D-*Fe*Co@NHC framework.

X-ray diffraction (XRD) is used to characterize the crystalline structure of the D-*Fe*Co@NHC catalyst. As shown in Fig. 2a, a wide peak at 26° is related to planes of graphite carbon (PDF#41–1487), and three diffraction peaks at 43, 51 and 76° correspond to the (111), (200), and (220) planes of Co (PDF#15–0806), respectively [34]. Notably, the diffraction peaks of D-*Fe*Co@NHC, D-*Fe*Co@NHC-3, and D-*Fe*Co@NHC-5
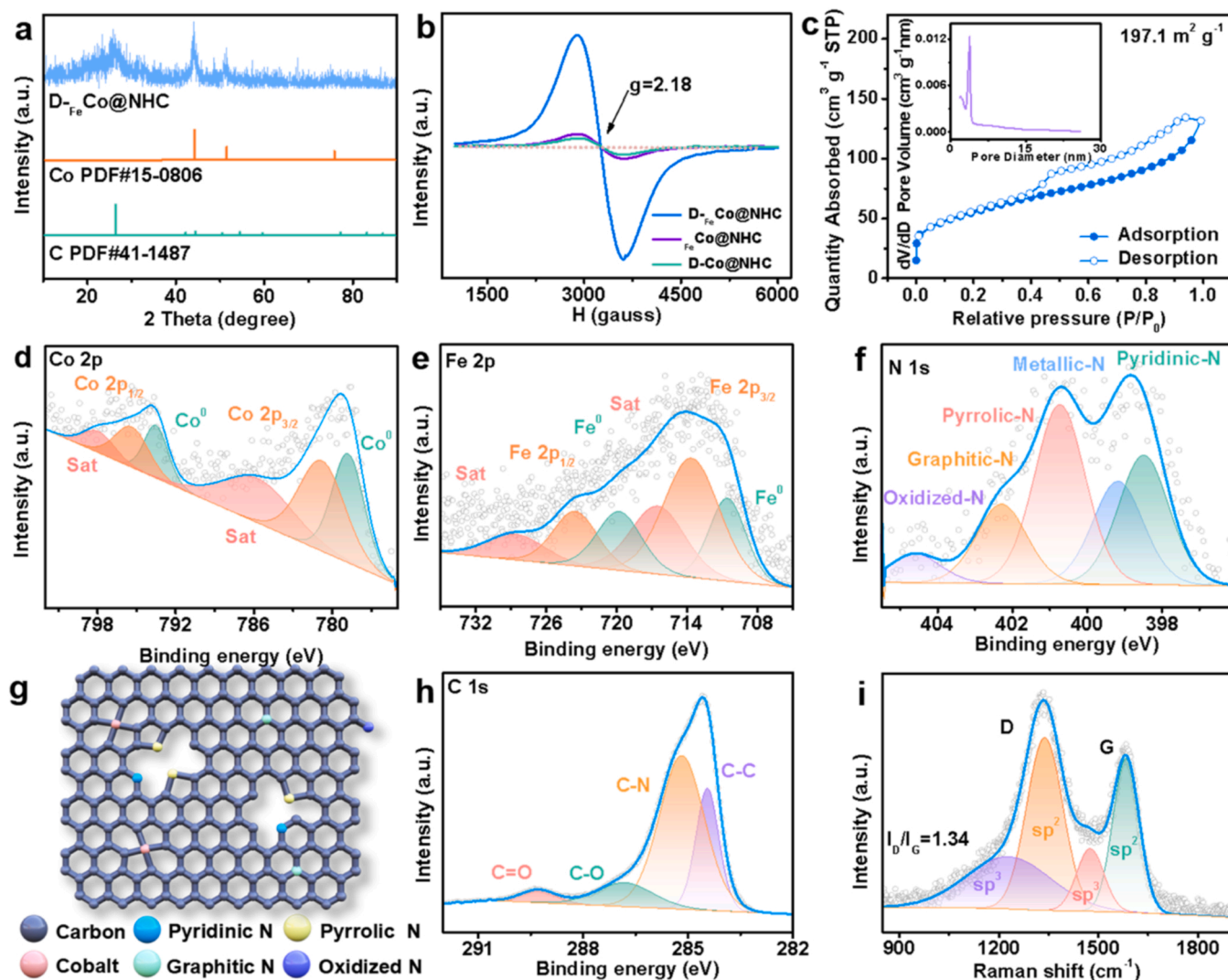
Fig. 2. a XRD patterns of D-*Fe*Co@NHC. **b** EPR spectra of D-*Fe*Co@NHC, *Fe*Co@NHC, and D-Co@NHC. **c** N_2 adsorption-desorption curve of D-*Fe*Co@NHC (Inset: pore diameter distribution). **d** Co 2p, **e** Fe 2p, **f** N 1s spectrum of D-*Fe*Co@NHC. **g** Diagrammatic illustration of N configuration, **h** C 1s XPS spectrum of D-*Fe*Co@NHC. **i** Raman spectrum with deconvoluted peaks of D-*Fe*Co@NHC.

are almost perfectly consistent with $_{Fe}$Co@NHC after acid soaking (Fig. S6-7). To ascertain the presence of defect in D-$_{Fe}$Co@NHC, electron paramagnetic resonance (EPR) spectra is conducted (Fig. 2b). Compared with $_{Fe}$Co@NHC and D-Co@NHC, the signal intensity of D-$_{Fe}$Co@NHC is obviously stronger at the g value of 2.18, revealing that Fe doping and acid soaking will promote the generation of metal defects. N_2 adsorption-desorption isotherm is applied to evaluate specific surface area and pore size of D-$_{Fe}$Co@NHC. As depicted in Fig. 2c, it demonstrates a typical type IV isotherm, where rapidly increase appears at low relative pressure (P/P_0 <0.05) and a unique hysteresis loop occurs at high relative pressure (P/P_0 >0.3). As a result, the measured specific surface area of D-$_{Fe}$Co@NHC is 197.1 $cm^2 \ g^{-1}$. The interpolated pore size distribution curve reveals that the pores is ranging from 0.5 to 10 nm (Fig. 2c inset), proving the coexistence of micropores and mesopores in the structure. The high specific surface area and rich pore structure make the active sites of the catalyst highly exposed, which is conducive to the maximum contact between electrolyte and active sites, and provides rich channels for the transport of ions in the electrolyte during ORR [35].

X-ray photoelectron spectroscopy (XPS) is used to detect the chemical composition and electronic structure of D-$_{Fe}$Co@NHC catalyst. The survey spectrum of D-$_{Fe}$Co@NHC demonstrate typical peaks of Co, Fe, N, C, and O (Fig. S8). In order to avoid the overlapping effect of Fe 2p on Co 2p, a standard Mg source is conducted to analyze the Co 2p, while other elements are analyzed with Al source [36]. The high resolution XPS spectrum of Co 2p (Fig. 2d) can be fitted into six peaks. Among these, peaks at 793.4 and 778.1 eV are ascribed to $Co^0 \ 2p_{1/2}$ and $Co^0 \ 2p_{3/2}$, and the peaks at 795.7 and 780.7 eV are related to $Co^{2+} \ 2p_{1/2}$ and $Co^{2+} \ 2p_{3/2}$, respectively, which indicate the coexistence of metallic cobalt and oxides on the surface of D-$_{Fe}$Co@NHC [37]. In addition, two Co satellite peaks at 799.2 and 785.0 eV are also observed. By comparing the Co 2p spectra of D-$_{Fe}$Co@NHC and D-Co@NHC (Fig. S9), it can be found that the binding energy of Co 2p in D-Co@NHC becomes higher, which indicates that Fe doping changes the electronic structure and electron redistribution promotes the process of electron transfer. The high-resolution XPS spectrum of Fe (Fig. 2e) demonstrate that two peaks at 720.5 and 710.8 eV are related to $Fe^0 \ 2p_{1/2}$ and $Fe^0 \ 2p_{3/2}$, and peaks at 723.4 and 713.5 eV are ascribed to $Fe^{2+} \ 2p_{1/2}$ and $Fe^{2+} \ 2p_{3/2}$, respectively. What's more, two satellite peaks of Fe are observed at 727.8 and 717.3 eV [38]. The N 1 s high-resolution spectrum of D-$_{Fe}$Co@NHC is on display in Fig. 2f, which can be divided into five peaks at 398.5, 399.2, 400.7, 402.3, 404.6 eV, corresponding to pyridinic N, metallic-N, pyrrolic N, graphitic N, and oxidized N, respectively [39]. The related nitrogen configuration is displayed in Fig. 2g. Different types of nitrogen doped in carbon matrix can change the electronic structure of catalysts and thereby improves the catalytic activity. To be specific, pyridinic N can accept electrons to transfer positive charges to adjacent sp^2 hybridized carbon atoms, which can facilitate the adsorption of reactants, and promoting the charge transfer between the reaction intermediates and the catalyst surface, and accelerating the ORR kinetics. In addition, pyrrolic N can regulate the metal sites in materials, and metallic N and graphitic N can provide more electrons and improve the conductivity of carbon-based materials. Moreover, the C 1s spectrum shows the existence of C=O groups (289.3 eV), C-C bonds (284.5 eV), C-N bonds (285.2 eV) and C-O bonds (286.1 eV) (Fig. 2h) [40]. The appearance of C-N bond is consistent with the result of N 1 s spectrum. The carbon characterizations of D-$_{Fe}$Co@NHC is further identified by Raman spectroscopy. As depicted in Fig. 2i, two wide peaks locate at 1331.3 and 1583.7 cm^{-1} are ascribed to disorder carbon (D-band) and graphitic carbon (G-band), respectively. In general, the relative peak intensity ratio of D and G band (I_D/I_G) is used to evaluate the disordering and graphitization degree of carbon species [41]. To be calculated, the I_D/I_G ratio of D-$_{Fe}$Co@NHC is 1.34, implying that the carbon in D-$_{Fe}$Co@NHC possess more defects. Furthermore, the above-mentioned two peaks can be divided into four peaks by Gaussian fitting. Among these, two peaks at 1338.7 and 1583.5 cm^{-1} belong to sp^2 type D-band

and G-band, and the other two peaks at 1229.0 and 1475.7 cm^{-1} correspond to sp^3 type carbon, respectively. The area ratio of sp^3/sp^2 in this catalyst is 60.2 %, which demonstrates that more sp^2 type carbon are existed in D-$_{Fe}$Co@NHC, and it will be conducive to the electron transfer. For comparison, Raman analysis on the $_{Fe}$Co@NHC sample without acid soaking is also carried out. As shown in Fig. S10, the intensity ratio (I_D/I_G) of D-band and G-band of $_{Fe}$Co@NHC is 0.94, which is significantly lower than that of D-$_{Fe}$Co@NHC. Therefore, it can be concluded that acid soaking will cause more defects on the carbon structure, which plays an important role in enhancing ORR activity.

3.2. Electrochemical activity evaluation

The electrochemical reduction performance of D-$_{Fe}$Co@NHC is firstly measured by cyclic voltammetry (CV) and linear sweep voltammetry (LSV) polarization experiments with a traditional three electrode system in 0.1 M KOH. The CV plot of D-$_{Fe}$Co@NHC shows an obvious reduction peak in O_2-saturated solution in comparison with N_2 atmosphere (Fig. S11a). Similar reduction peaks also appear in the sample of D-$_{Fe}$Co@NHC-3, D-$_{Fe}$Co@NHC-5, $_{Fe}$Co@NHC, and D-Co@NHC (Fig. S11b), indicating that these catalysts possess potential of electrocatalysis activity for ORR. As shown in Fig. 3a, D-$_{Fe}$Co@NHC displays excellent ORR performance with $E_{1/2}$ of about 0.8512 V, which is comparable to that of commercial Pt/C, outperforming than the D-$_{Fe}$Co@NHC-3, D-$_{Fe}$Co@NHC-5, $_{Fe}$Co@NHC, and D-Co@NHC (Fig. S12). Furthermore, the kinetic current density (J_K) of D-$_{Fe}$Co@NHC (0.901 mA cm^{-2}) at 0.9 V is larger than that of $_{Fe}$Co@NHC (0.423 mA cm^{-2}), D-Co@NHC (0.335 mA cm^{-2}), which is similar to that of Pt/C (1.080 mA cm^{-2}), indicating a faster reaction kinetics and effective pervasion of reactants for D-$_{Fe}$Co@NHC electrocatalysts. Meanwhile also reflects that the catalyst has excellent ORR catalytic activity (Fig. 3b) [42–44]. The Tafel slope of D-$_{Fe}$Co@NHC is as low as 48.7 mV dec^{-1} (Fig. 3c, Fig. S13), demonstrating the accelerated ORR dynamics. Impressively, D-$_{Fe}$Co@NHC exhibits superior ORR performance to those of recently reported ORR catalysts (Fig. 3d and Table S2). To further study the ORR mechanism, LSV curves of D-$_{Fe}$Co@NHC with different rotation speeds are tested and the related Koutechy-Levich (K-L) plots are recorded in Fig. 3e. To be calculated, the K-L curves show a fine linear relationship at increasing potentials and the electron transfer number (n) is about 4.0, indicating a four-electron transfer path during ORR process. In addition, intermediate peroxide (H_2O_2) product is evaluated by a rotating ring-disk electrodes (RRDE). As displayed in Fig. S14, the yield of H_2O_2 is approximately 10 %, and the corresponding n is calculated to be about 4.0, which is consistent with the results calculated by K-L plots.

Seawater contains a variety of dissolved ions, such as chloride ion, which may make an impact to the catalytic reaction of air electrodes and the overall battery performance [45]. Therefore, it is of great significance to determine the influence mechanism of Cl⁻ in seawater on ORR activity. In this work, we use simulated seawater, namely 0.1 M KOH + x M NaCl (x = 0, 0.2, 0.5, 1.0), to test the ORR performance of D-$_{Fe}$Co@NHC and Pt/C. As the concentration of NaCl increase from 0 M to 1.0 M, the $E_{1/2}$ of D-$_{Fe}$Co@NHC does not change significantly, but it limiting current density gets smaller (Fig. 3 f), and Pt/C also shows a similar trend (Fig. S15). For subsequent ORR test, 0.1 M KOH + seawater is used as electrolyte. As can be seen from Fig. 3 g, D-$_{Fe}$Co@NHC afford an impressive ORR activity with $E_{1/2}$ of 0.874 V, which is comparable to that of commercial Pt/C (0.880 V). It should be noted the ORR activity is quite different in 0.1 M KOH + seawater and 0.1 M KOH. On one hand, the $E_{1/2}$ of the electrocatalysts measured in 0.1 M KOH + seawater is significantly improved. This may be related to the abundant soluble ions in seawater, which can effectively accelerate the charge transfer. On the other hand, the limiting current density decay slightly in 0.1 M KOH + seawater, which may attribute to the appearance of Cl⁻ in seawater. In addition, we further explored the CV, K-L curves and H_2O_2 yield in 0.1 M KOH + seawater and 0.1 M
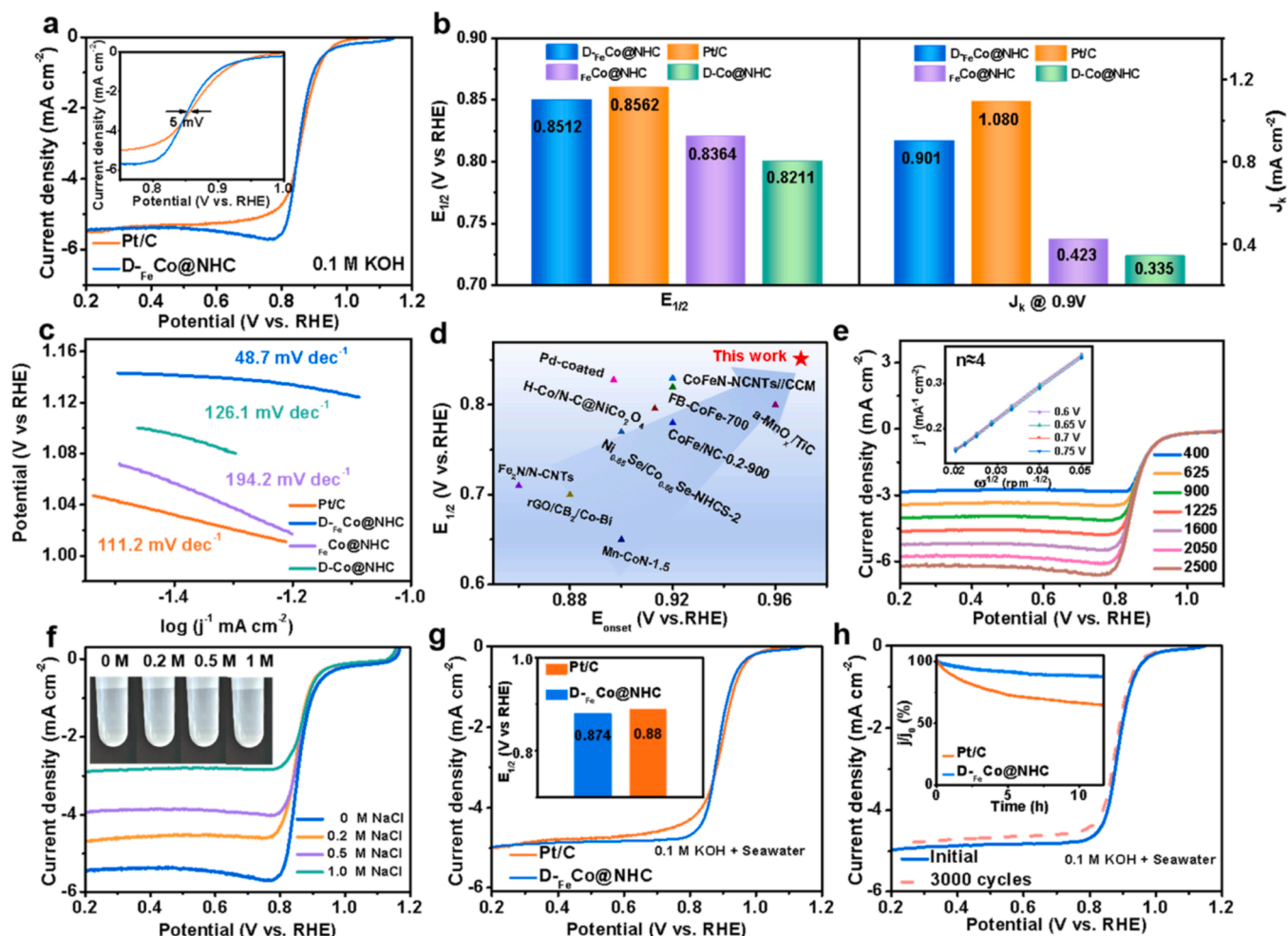
Fig. 3. a LSV curves of D-$_{Fe}$Co@NHC and Pt/C for ORR in 0.1 M KOH solution at 1600 rpm. (inset: comparison diagram of the $E_{1/2}$), **b** $E_{1/2}$ and J_K at 0.9 V, and **c** corresponding Tafel slopes of D-$_{Fe}$Co@NHC, $_{Fe}$Co@NHC, D-Co@NHC, Pt/C, **d** Compared of E_{onset} and $E_{1/2}$ of D-$_{Fe}$Co@NHC with the previously reported ORR catalysts in 0.1 M KOH. **e** ORR polarization curves at different rpm (inset is a fitting diagram of K-L equation at different voltages) in 0.1 M KOH. **f** ORR LSV curves of D-$_{Fe}$Co@NHC in 0.1 M KOH + x M NaCl (x = 0, 0.2, 0.5, and 1.0) electrolytes (inset: optical photographs of various electrolytes). **g** LSV curves of D-$_{Fe}$Co@NHC and Pt/C for ORR in 0.1 M KOH + seawater at 1600 rpm (inset is the bar diagram of the $E_{1/2}$). **h** ORR durability test in 1.0 M KOH + seawater.

KOH+ 0.5 M NaCl, confirming a four-electron transfer path in these different solutions (Fig. S16).

Apart from the catalytic activity, stability is another important criterion for ORR in practical applications. As can be seen from Fig. 3 h, the LSV curve of D-$_{Fe}$Co@NHC displays negligible variation compared to the initial one after 3000 CV cycles in 0.1 M KOH + seawater. What's more, 88 % of the initial current is maintained after 12 h i-t testing, outperforming the commercial Pt/C with 64 % retention of the current density (Fig. 3 h inset), proving the excellent stability of the D-$_{Fe}$Co@NHC catalyst towards ORR. Different electrolytes of 0.1 M KOH and 0.1 M KOH + 0.5 M NaCl are also adopted to test the durability of D-$_{Fe}$Co@NHC (Fig. S17). The structure information of D-$_{Fe}$Co@NHC after ORR durability test is characterized by SEM and XRD, and no obvious changes in morphology and composition (Fig. S18). Moreover, the XPS spectra of Co 2p (Fig. S19a) and Fe 2p (Fig. S19b) also have no significant shift after ORR test. All above-mentioned results verify that the excellent durability of D-$_{Fe}$Co@NHC as ideal ORR electrocatalyst.

3.3. Density functional theory (DFT) calculation

In order to provide deeper insights into the catalytic mechanism of D-$_{Fe}$Co@NHC and to explore the intrinsic factors for the good ORR activity, three different models of D-$_{Fe}$Co//D-NC, D-$_{Fe}$Co//C and $_{Fe}$Co//D-NC were constructed through density functional theory (DFT) (Fig. S20).

D-$_{Fe}$Co//D-NC represent the as-prepared D-$_{Fe}$Co@NHC, and the D-$_{Fe}$Co//C and $_{Fe}$Co//D-NC represent the only metal defect and only carbon defect, respectively. As for D-$_{Fe}$Co//D-NC, the Fe atoms is located in the lattice of Co. According to the Bader charge analysis of Fig. 4a and Fig. S21, it can be seen that metal defects lead to changes in the valence bonds between adjacent atomic charges, in particular, the metal clusters transfer 0.848, 0.714 and 0.845 electrons to the carbon support of D-$_{Fe}$Co//D-NC, D-$_{Fe}$Co//C and $_{Fe}$Co//D-NC, respectively, resulting in the modulation of electronic structure [46,47]. To illustrate the localization distribution of electrons, the charge density difference and electronic local function (ELF) of D-$_{Fe}$Co//D-NC in Fig. 4b-c indicate that electrons are mostly present at the interface, and there is a strong interaction between D-$_{Fe}$Co clusters and NC, which plays an important role in promoting charge transfer during ORR process. To further study the electronic migration, the internal reasons for the enhancement of catalyst activity are analyzed by work function analysis (Fig. 4d and Fig. S22). The lower the work function, less energy is required to transfer electrons from inside the catalyst to the surface [48,49]. The work function of D-$_{Fe}$Co//D-NC is 4.366 eV, which is lower than that of D-$_{Fe}$Co//C (4.476 eV) and $_{Fe}$Co//D-NC (4.424 eV), indicating that the metal and carbon defects can synergistically promote electrons spill from the inside of the metal to the surface of catalyst. Moreover, the probability of electron transition to antibonding bands will decrease when the D-band center of the transition metal atom is increased relative to the Fermi
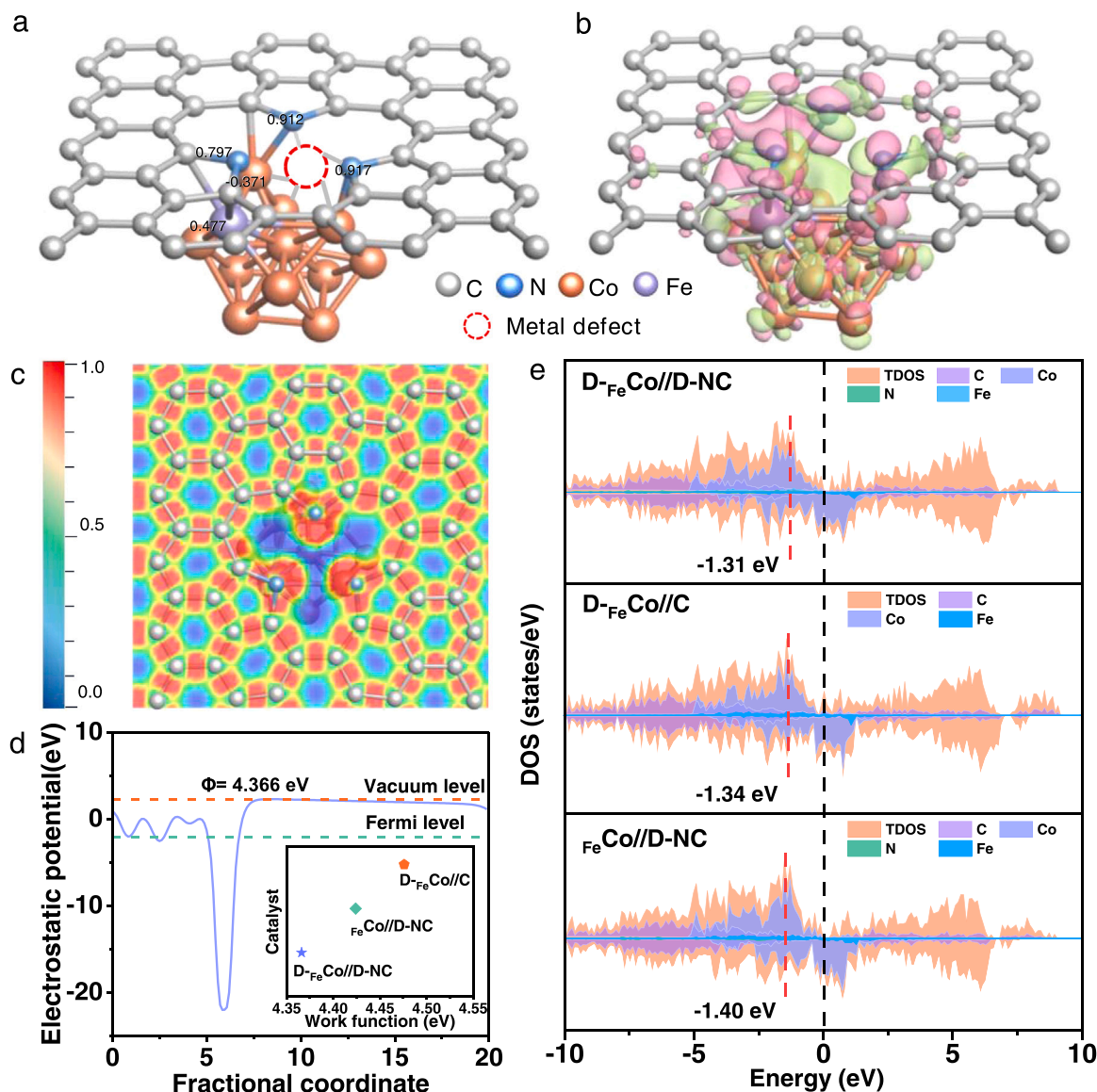
Fig. 4. a Bader charge analysis (The red circle is a metal defect of Co), **b** Charge density difference analysis, and **c** the ELF of D-$_{Fe}$Co//D-NC. **d** Computed work functions of D-$_{Fe}$Co//D-NC. **e** DOS of D-$_{Fe}$Co//D-NC, D-$_{Fe}$Co//C, $_{Fe}$Co//D-NC.

level (E_f = 0 eV), resulting in a decrease in the adsorption strength between the adsorbate and transition metal, and vice versa. Fig. 4e shows the total density of states (TDOS) and the corresponding D-band center values of three models. It is worth noting that the calculated value of the D-band center corresponding to the Fermi level of the three models of $_{Fe}$Co//D-NC, D-$_{Fe}$Co//C and D-$_{Fe}$Co//D-NC is 1.40, 1.34, 1.31 eV, respectively. Due to the existence of rich metal and carbon defects, the D-band center is moved up, and the adsorption strength is enhanced, which can promote the adsorption of O_2 and more oxygen can be adsorbed to the defect sites, increasing the contact area between the catalyst and oxygen and accelerating the mass transfer process, thus enhancing the intrinsic ORR activity [50,51].

3.4. Zinc-air battery

The excellent ORR performance of D-$_{Fe}$Co@NHC in alkaline seawater provides possibility for its application in ZAB [52]. By using alkaline seawater as electroyte, the assembled ZAB with D-$_{Fe}$Co@NHC as air cathode displays higher open circuit voltage (1.48 V) than that of commercial Pt/C (1.44 V) (Fig. 5a). The related discharge polarization

curve and power density curve of the assembled ZAB are shown in Fig. 5b, it can be seen that D-$_{Fe}$Co@NHC display a higher peak power density (173 mW cm^{-2}) in comparison with commercial Pt/C. The discharge test under different current densities (2, 5, 10, 20 and 30 mA cm^{-2}) demonstrate that D-$_{Fe}$Co@NHC possess a better rate capability compared to commercial Pt/C (Fig. S23). Additionally, the specific discharge capacities of D-$_{Fe}$Co@NHC-based ZAB are determined to be 782.7, 750.8 and 700.3 mAh g^{-1} (when normalized to the mass of consumed Zn anode) at 5, 10 and 20 mA cm^{-2} (Fig. S24). To evaluate the cycle stability of D-$_{Fe}$Co@NHC based ZAB, the continuous constant current discharge-charge test are conducted under the current density of 10 mA cm^{-2} (Fig. 5c). As a result, the ZAB catalyzed by D-$_{Fe}$Co@NHC displays a cycling capacity of up to 800 h, and the voltage difference change is only 0.82 V, proving the excellent stability of the D-$_{Fe}$Co@NHC in alkaline seawater. For comparison, the ZAB performance is also carried out with simulated seawater as electrolyte (Fig. S25 and Fig. S26). ZAB with D-$_{Fe}$Co@NHC as air cathode shows excellent electrochemical performance both in seawater electrolyte or simulated seawater electrolyte, indicating the strong ability for resistance corrosion of D-$_{Fe}$Co@NHC in complex seawater solution.
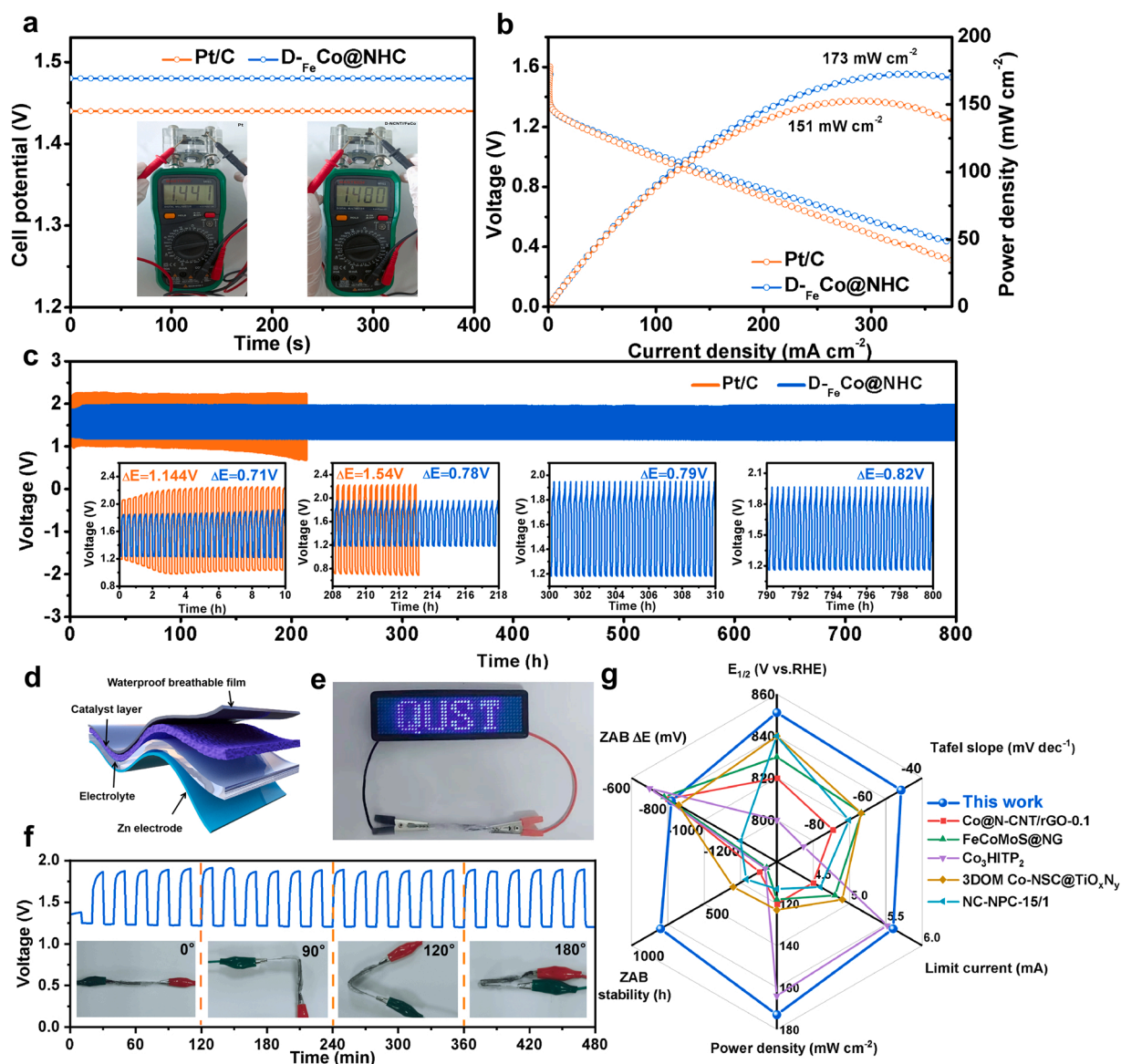
Fig. 5. a Open circuit voltage, **b** discharge polarization curves and related power density curves, and **c** galvanostatic discharge-charge cycling stability of liquid ZAB with D-$_{Fe}$Co@NHC and Pt/C catalysts as air cathode, respectively. **d** the schematic diagram of the flexible ZAB. **e** Photos of LEDs powered by flexible ZAB, and **f** Cycling test in mimicking real bending circumstances of flexible ZAB with D-$_{Fe}$Co@NHC as air cathode. **g** Comprehensive comparison of the performance of D-$_{Fe}$Co@NHC and other reported state-of-the-art catalysts.

In addition, flexible quasi-solid-state ZAB with D-$_{Fe}$Co@NHC as cathode was assembled, and its schematic diagram is shown in Fig. 5d. It should be noted that the quasi-solid-state electrolyte is based on alkaline seawater with polyvinyl alcohol (PVA). As depicted in Fig. 5e, one flexible ZAB can supply enough power to light up a light emitting diode (LED) panel. Additionally, the flexible ZAB has high mechanical flexibility, the charge and discharge platform kept stable at different bending angles of from 0° to 180° (Fig. 5f). More importantly, the ZABs performance of D-$_{Fe}$Co@NHC is superior to many previously reported catalysts (Fig. 5g, Table S3 and S4).

4. Conclusions

In summary, we have developed a facile strategy to construct defect-rich Fe-doped Co nanoparticles encapsulated by N-doped hierarchical carbon (D-$_{Fe}$Co@NHC), which was used as ORR electrocatalyst in seawater-based electrolyte. Notably, the Fe doping not only helps to promote the generation of metal defect, but also adjust the electronic

structure of D-$_{Fe}$Co@NHC. DFT calculations indicate that the metal defect and carbon defect jointly optimize the D-band center of D-$_{Fe}$Co@NHC to boost the ORR performance. As a result, in alkaline seawater electrolyte, the as-prepared D-$_{Fe}$Co@NHC exhibit a high $E_{1/2}$ of 0.874 V, and the assembled liquid ZAB show a high peak power density of 173 mW cm^{-2} and ultra-long cycling stability over 800 h. In addition, the D-$_{Fe}$Co@NHC also exhibits great potential as an air cathode for seawater-based flexible quasi-solid-state ZAB. This work opens a new avenue for the design and synthesis of non-noble metal electrocatalysts for ORR in seawater electrolytes.

Declaration of Competing Interest

The authors declare that they have no known competing financial interests or personal relationships that could have appeared to influence the work reported in this paper.

Data Availability

No data was used for the research described in the article.

Acknowledgement

Appendix A. Supporting information

Supplementary data associated with this article can be found in the online version at doi:10.1016/j.apcatb.2023.122634.

References

[1] S. Luo, Z. Zeng, H. Wang, W. Xiong, B. Song, C. Zhou, A. Duan, X. Tan, Q. He, G. Zeng, Z. Liu, R. Xiao, Recent progress in conjugated microporous polymers for clean energy: synthesis, modification, computer simulations, and applications, Prog. Polym. Sci. 115 (2021), 101374, https://doi.org/10.1016/j.progpolymsci.2021.101374.

[2] J. Chen, C. Fan, X. Hu, C. Wang, Z. Huang, G. Fu, J.M. Lee, Y. Tang, Hierarchically porous Co/Co(x) M(y) (M = P, N) as an efficient Mott-Schottky electrocatalyst for oxygen evolution in rechargeable Zn-Air batteries, Small 15 (2019), e1901518, https://doi.org/10.1002/smll.201901518.

[3] N.K. Wagh, S.S. Shinde, C.H. Lee, S.H. Kim, D.H. Kim, H.D. Um, S.U. Lee, J.H. Lee, Supramolecular polymer intertwined free-standing bifunctional membrane catalysts for all-temperature flexible Zn-air batteries, Nano-Micro Lett. 14 (2022) 190, https://doi.org/10.1007/s40820-022-00927-0.

[4] G. Fu, J. Wang, Y. Chen, Y. Liu, Y. Tang, J.B. Goodenough, J.-M. Lee, Exploring indium-based ternary thiospinel as conceivable high-potential air-cathode for rechargeable Zn-air batteries, Adv. Energy Mater. 8 (2018) 1802263, https://doi.org/10.1002/aenm.201802263.

[5] X. Hu, Y. Chen, M. Zhang, G. Fu, D. Sun, J.-M. Lee, Y. Tang, Alveolate porous carbon aerogels supported Co9S8 derived from a novel hybrid hydrogel for bifunctional oxygen electrocatalysis, Carbon 144 (2019) 557–566, https://doi.org/10.1016/j.carbon.2018.12.099.

[6] G. Fu, Y. Wang, Y. Tang, K. Zhou, J.B. Goodenough, J.-M. Lee, Superior oxygen electrocatalysis on nickel indium thiospinels for rechargeable Zn-air batteries, ACS Mater. Lett. 1 (2019) 123–131, https://doi.org/10.1021/acsmaterialslett.9b00093.

[7] T.Y. Jeon, S.H. Yu, S.J. Yoo, H.Y. Park, S.K. Kim, Electrochemical determination of the degree of atomic surface roughness in Pt–Ni alloy nanocatalysts for oxygen reduction reaction, Carbon Energy 3 (2020) 375–383, https://doi.org/10.1002/cey2.82.

[8] X. Qin, D. Kim, Y. Piao, Metal-organic frameworks-derived novel nanostructured electrocatalysts for oxygen evolution reaction, Carbon Energy 3 (2020) 66–100, https://doi.org/10.1002/cey2.80.

[9] V. Jose, H. Hu, E. Edison, W. Manalastas, Jr, H. Ren, P. Kidkhunthod, S. Sreejith, A. Jayakumar, J.M.V. Nsanzimana, M. Srinivasan, J. Choi, J.M. Lee, Modulation of single atomic Co and Fe sites on hollow carbon nanospheres as oxygen electrodes for rechargeable Zn-Air batteries, Small Methods 5 (2021), e2000751, https://doi.org/10.1002/smtd.202000751.

[10] G. Fu, X. Yan, Y. Chen, L. Xu, D. Sun, J.M. Lee, Y. Tang, Boosting bifunctional oxygen electrocatalysis with 3D graphene aerogel-supported Ni/MnO particles, Adv. Mater. 30 (2018) 1704609, https://doi.org/10.1002/adma.201704609.

[11] S.T. Senthilkumar, S.O. Park, J. Kim, S.M. Hwang, S.K. Kwak, Y. Kim, Seawater battery performance enhancement enabled by a defect/edge-rich, oxygen self-doped porous carbon electrocatalyst, J. Mater. Chem. A 5 (2017) 14174–14181, https://doi.org/10.1039/c7ta03298f.

[12] J. Yu, B.-Q. Li, C.-X. Zhao, Q. Zhang, Seawater electrolyte-based metal–air batteries: from strategies to applications, Energy Environ. Sci. 13 (2020) 3253–3268, https://doi.org/10.1039/d0ee01617a.

[13] Q. Zhao, Y. Wang, W.-H. Lai, F. Xiao, Y. Lyu, C. Liao, M. Shao, Approaching a high-rate and sustainable production of hydrogen peroxide: oxygen reduction on Co–N–C single-atom electrocatalysts in simulated seawater, Energy Environ. Sci. 14 (2021) 5444–5456, https://doi.org/10.1039/d1ee00878a.

[14] Q. Zhang, X. Zhao, X. Miao, W. Yang, C. Wang, Q. Pan, ZIF-L-Co@carbon fiber paper composite derived Co/Co3O4@C electrocatalyst for ORR in alkali/acidic

[15] Y. Li, C.K. Peng, H. Hu, S.Y. Chen, J.H. Choi, Y.G. Lin, J.M. Lee, Interstitial boron-triggered electron-deficient Os aerogels for enhanced pH-universal hydrogen evolution, Nat. Commun. 13 (2022) 1143, https://doi.org/10.1038/s41467-022-28805-8.

[16] X. Liu, H. Mao, G. Liu, Q. Yu, S. Wu, B. Li, G. Zhou, Z. Li, L. Wang, Metal doping and Hetero-engineering of Cu-doped CoFe/Co embedded in N-doped carbon for improving trifunctional electrocatalytic activity in alkaline seawater, Chem. Eng. J. 451 (2023), 138699, https://doi.org/10.1016/j.cej.2022.138699.

[17] S. Kim, S. Ji, H. Yang, H. Son, H. Choi, J. Kang, O.L. Li, Near surface electric field enhancement: Pyridinic-N rich few-layer graphene encapsulating cobalt catalysts as highly active and stable bifunctional ORR/OER catalyst for seawater batteries, Appl. Catal. B Environ. 310 (2022), 121361, https://doi.org/10.1016/j.apcatb.2022.121361.

[18] J. Zhang, J. Zhang, F. He, Y. Chen, J. Zhu, D. Wang, S. Mu, H.Y. Yang, Defect and doping Co-engineered non-metal nanocarbon ORR electrocatalyst, Nano-Micro Lett. 13 (2021) 65, https://doi.org/10.1007/s40820-020-00579-y.

[19] J. Zhang, J. Zheng, Z. Tang, D. Bi, J. Zhao, Y. Liang, Optimal configuration of N-doped carbon defects in 2D turbostratic carbon nanomesh for advanced oxygen reduction electrocatalysis, Angew. Chem. Int. Ed. 59 (2020) 11999–12006, https://doi.org/10.1002/anie.202000936.

[20] Q. Wu, Q. Liu, Y. Zhou, Y. Sun, J. Zhao, Y. Liu, F. Liu, M. Nie, F. Ning, N. Yang, X. Jiang, X. Zhou, J. Zhong, Z. Kang, Carbon defect-induced reversible carbon-oxygen interfaces for efficient oxygen reduction, ACS Appl. Mater. Interfaces 10 (2018) 39735–39744, https://doi.org/10.1021/acsami.8b14323.

[21] K. Li, R. Zhang, R. Gao, G.-Q. Shen, L. Pan, Y. Yao, K. Yu, X. Zhang, J.-J. Zou, Metal-defected spinel MnxCo3−xO4 with octahedral Mn-enriched surface for highly efficient oxygen reduction reaction, Appl. Catal. B Environ. 244 (2019) 536–545, https://doi.org/10.1016/j.apcatb.2018.11.072.

[22] J. Li, D. Wang, R. Guan, Y. Zhang, Z. Zhao, H. Zhai, Z. Sun, Vacancy-enabled mesoporous TiO2 modulated by nickel doping with enhanced photocatalytic nitrogen fixation performance, ACS Sustain. Chem. Eng. 8 (2020) 18258–18265, https://doi.org/10.1021/acssuschemeng.0c06775.

[23] P. Su, W. Huang, J. Zhang, U. Guharoy, Q. Du, Q. Sun, Q. Jiang, Y. Cheng, J. Yang, X. Zhang, Y. Liu, S.P. Jiang, J. Liu, Fe atoms anchored on defective nitrogen doped hollow carbon spheres as efficient electrocatalysts for oxygen reduction reaction, Nano Res. 14 (2020) 1069–1077, https://doi.org/10.1007/s12274-020-3151-8.

[24] V. Jose, J.M.V. Nsanzimana, H. Hu, J. Choi, X. Wang, J.M. Lee, Highly efficient oxygen reduction reaction activity of N-doped carbon–cobalt boride heterointerfaces, Adv. Energy Mater. 11 (2021) 2100157, https://doi.org/10.1002/aenm.202100157.

[25] P. Prabhu, J.M. Lee, Metallenes as functional materials in electrocatalysis, Chem. Soc. Rev. 50 (2021) 6700–6719, https://doi.org/10.1039/d0cs01041c.

[26] P. Rao, T.-J. Wang, J. Li, P.-L. Deng, Y.-J. Shen, Y. Chen, X.-L. Tian, Plasma induced Fe-N active sites to improve the oxygen reduction reaction performance, Adv. Sens. Energy Mater. 1 (2022), 100005, https://doi.org/10.1016/j.asems.2022.100005.

[27] P. Rao, D. Wu, T.-J. Wang, J. Li, P. Deng, Q. Chen, Y. Shen, Y. Chen, X. Tian, Single atomic cobalt electrocatalyst for efficient oxygen reduction reaction, eScience 2 (2022) 399–404, https://doi.org/10.1016/j.esci.2022.05.004.

[28] P. Prabhu, V. Jose, J.-M. Lee, Design strategies for development of TMD-based heterostructures in electrochemical energy systems, Matter 2 (2020) 526–553, https://doi.org/10.1016/j.matt.2020.01.001.

[29] C.C. Yang, S.F. Zai, Y.T. Zhou, L. Du, Q. Jiang, Fe3C-Co nanoparticles encapsulated in a hierarchical structure of N-doped carbon as a multifunctional electrocatalyst for ORR, OER, and HER, Adv. Funct. Mater. (2019) 1901949, https://doi.org/10.1002/adfm.201901949.

[30] H. Wang, J. Li, K. Li, Y. Lin, J. Chen, L. Gao, V. Nicolosi, X. Xiao, J.M. Lee, Transition metal nitrides for electrochemical energy applications, Chem. Soc. Rev. 50 (2021) 1354–1390, https://doi.org/10.1039/d0cs00415d.

[31] Q. Zhou, Y. Chen, G. Zhao, Y. Lin, Z. Yu, X. Xu, S. Wang, H.K. Liu, W. Sun, S. X. Dou, Active-site-enriched iron-doped nickel/cobalt hydroxide nanosheets for enhanced oxygen evolution reaction, ACS Catal. 8 (2018) 5382–5390, https://doi.org/10.1021/acscatal.8b01332.

[32] Z. Sun, A. Curto, J. Rodriguez-Fernandez, Z. Wang, A. Parikh, J. Fester, M. Dong, A. Vojvodic, J.V. Lauritsen, The effect of Fe dopant location in Co(Fe)OOHx nanoparticles for the oxygen evolution reaction, ACS Nano (2021) 18226–18236, https://doi.org/10.1021/acsnano.1c07219.

[33] G. Zhou, G. Liu, X. Liu, Q. Yu, H. Mao, Z. Xiao, L. Wang, 1D/3D heterogeneous assembling body as trifunctional electrocatalysts enabling zinc–air battery and self-powered overall water splitting, Adv. Funct. Mater. 32 (2021) 2107608, https://doi.org/10.1002/adfm.202107608.

[34] Y. Ha, B. Fei, X. Yan, H. Xu, Z. Chen, L. Shi, M. Fu, W. Xu, R. Wu, Atomically dispersed Co-pyridinic N-C for superior oxygen reduction reaction, Adv. Energy Mater. 10 (2020) 2002592, https://doi.org/10.1002/aenm.202002592.

[35] X. Liu, Y. Zhang, Z. Zhao, H. Gao, J. Kang, R. Wang, G. Ge, X. Jia, Highly exposed discrete Co atoms anchored in ultrathin porous N, P-codoped carbon nanosheets for efficient oxygen electrocatalysis and rechargeable aqueous/solid-state Zn–air batteries, J. Mater. Chem. A 9 (2021) 22643–22652, https://doi.org/10.1039/d1ta07404k.

[36] S. Diodati, L. Pandolfo, A. Caneschi, S. Gialanella, S. Gross, Green and low temperature synthesis of nanocrystalline transition metal ferrites by simple wet chemistry routes, Nano Res. 7 (2014) 1027–1042, https://doi.org/10.1007/s12274-014-0466-3.

[37] Y. Xue, Y. Guo, Q. Zhang, Z. Xie, J. Wei, Z. Zhou, MOF-derived Co and Fe species loaded on N-doped carbon networks as efficient oxygen electrocatalysts for Zn-Air

batteries, Nano-Microb.Lett. 14 (2022) 162, https://doi.org/10.1007/s40820-022-00890-w.

[38] M. Zhao, H. Liu, H. Zhang, W. Chen, H. Sun, Z. Wang, B. Zhang, L. Song, Y. Yang, C. Ma, Y. Han, W. Huang, A pH-universal ORR catalyst with single-atom iron sites derived from a double-layer MOF for superior flexible quasi-solid-state rechargeable Zn–air battery, Energy Environ. Sci. 14 (2021) 6455–6463, https://doi.org/10.1039/d1ee01602d.

[39] Y. Gao, D. Kong, F. Cao, S. Teng, T. Liang, B. Luo, B. Wang, Q.-H. Yang, L. Zhi, Synergistically tuning the graphitic degree, porosity, and the configuration of active sites for highly active bifunctional catalysts and Zn-air batteries, Nano Res. (2022) 1–9, https://doi.org/10.1007/s12274-022-4497-x.

[40] Z.-Y. Mei, S. Cai, G. Zhao, Q. Jing, X. Sheng, J. Jiang, H. Guo, Understanding electronic configurarions and coordination environment for enhanced ORR process and improved Zn-air battery performance, Energy Storage Mater. 50 (2022) 12–20, https://doi.org/10.1016/j.ensm.2022.05.006.

[41] F. Wang, N. Zhang, X. Zhao, L. Wang, J. Zhang, T. Wang, F. Liu, Y. Liu, L.Z. Fan, Realizing a high-performance Na-storage cathode by tailoring ultrasmall Na2FePO4F nanoparticles with facilitated reaction kinetics, Adv. Sci 6 (2019) 1900649, https://doi.org/10.1002/advs.201900649.

[42] W. Chen, Q. Xiang, T. Peng, C. Song, W. Shang, T. Deng, J. Wu, Reconsidering the benchmarking evaluation of catalytic activity in oxygen reduction reaction, iScience 23 (2020), 101532, https://doi.org/10.1016/j.isci.2020.101532.

[43] J. Wang, C.-X. Zhao, J.-N. Liu, D. Ren, B.-Q. Li, J.-Q. Huang, Q. Zhang, Quantitative kinetic analysis on oxygen reduction reaction: a perspective, Nano Mater. Sci. 3 (2021) 313–318, https://doi.org/10.1016/j.nanoms.2021.03.006.

[44] S. Xu, Y. Kim, D. Higgins, M. Yusuf, T.F. Jaramillo, F.B. Prinz, Building upon the Koutecky-Levich equation for evaluation of next-generation oxygen reduction reaction catalysts, Electrochim. Acta 255 (2017) 99–108, https://doi.org/10.1016/j.electacta.2017.09.145.

[45] J. Yu, C.-X. Zhao, J.-N. Liu, B.-Q. Li, C. Tang, Q. Zhang, Seawater-based electrolyte for Zinc–air batteries, Green Chem. Eng. 1 (2020) 117–123, https://doi.org/10.1016/j.gce.2020.09.013.

[46] Y. Qin, M. Yang, C. Deng, W. Shen, R. He, M. Li, Theoretical insight into single Rh atoms anchored on N-doped gamma-graphyne as an excellent bifunctional electrocatalyst for the OER and ORR: electronic regulation of graphitic nitrogen, Nanoscale 13 (2021) 5800–5808, https://doi.org/10.1039/d0nr07513b.

[47] M. Rittiruam, S. Somdee, P. Buapin, N. Aumnongpho, N. Kerdprasit, T. Saelee, S. Kheawhom, N. Chotigkrai, S. Praserthdam, P. Praserthdam, On the deactivation mechanisms of MnO2 electrocatalyst during operation in rechargeable zinc-air batteries studied via density functional theory, J. Alloy. Compd. 869 (2021), 159280, https://doi.org/10.1016/j.jallcom.2021.159280.

[48] X. Wang, W. Zhang, Q. Yu, X. Liu, Q. Liang, X. Meng, X. Wang, L. Wang, Fe-doped CoNiP@N-doped carbon nanosheet arrays for hydrazine oxidation assisting energy-saving seawater splitting, Chem. Eng. J. 446 (2022) 136987, https://doi.org/10.1016/j.cej.2022.136987.

[49] W. Zhang, X. Liu, Q. Yu, X. Wang, H. Mao, J. Chi, B. Li, J. Wan, L. Wang, In situ electronic redistribution of Ni2P hierarchical structure for energy-saving hydrogen production in seawater, Chem. Eng. J. 454 (2023), 140210, https://doi.org/10.1016/j.cej.2022.140210.

[50] Y. Han, Y. Wang, R. Xu, W. Chen, L. Zheng, A. Han, Y. Zhu, J. Zhang, H. Zhang, J. Luo, C. Chen, Q. Peng, D. Wang, Y. Li, Electronic structure engineering to boost oxygen reduction activity by controlling the coordination of the central metal, Energy Environ. Sci. 11 (2018) 2348–2352, https://doi.org/10.1039/c8ee01481g.

[51] Y. Mun, S. Lee, K. Kim, S. Kim, S. Lee, J.W. Han, J. Lee, Versatile strategy for tuning ORR activity of a single Fe-N(4) site by controlling electron-withdrawing/donating properties of a carbon plane, J. Am. Chem. Soc. 141 (2019) 6254–6262, https://doi.org/10.1021/jacs.8b13543.

[52] Y. Han, H. Duan, C. Zhou, H. Meng, Q. Jiang, B. Wang, W. Yan, R. Zhang, Stabilizing cobalt single atoms via flexible carbon membranes as bifunctional electrocatalysts for binder-free zinc-air batteries, Nano Lett. 22 (2022) 2497–2505, https://doi.org/10.1021/acs.nanolett.2c00278.